

# Soliton-dependent plasmon reflection at bilayer graphene domain walls

Lili Jiang<sup>1,2†</sup>, Zhiwen Shi<sup>1†</sup>, Bo Zeng<sup>1</sup>, Sheng Wang<sup>1</sup>, Ji-Hun Kang<sup>1</sup>, Trinity Joshi<sup>1</sup>, Chenhao Jin<sup>1</sup>, Long Ju<sup>1</sup>, Jonghwan Kim<sup>1</sup>, Tairu Lyu<sup>3</sup>, Yuen-Ron Shen<sup>1,4</sup>, Michael Crommie<sup>1,4,5</sup>, Hong-Jun Gao<sup>2</sup> and Feng Wang<sup>1,4,5\*</sup>

**Layer-stacking domain walls in bilayer graphene are emerging as a fascinating one-dimensional system<sup>1–11</sup> that features stacking solitons<sup>1–4</sup> structurally and quantum valley Hall boundary states<sup>5–11</sup> electronically. The interactions between electrons in the 2D graphene domains and the one-dimensional domain-wall solitons can lead to further new quantum phenomena. Domain-wall solitons of varied local structures exist along different crystallographic orientations<sup>1,2,12,13</sup>, which can exhibit distinct electrical, mechanical and optical properties. Here we report soliton-dependent 2D graphene plasmon reflection at different 1D domain-wall solitons in bilayer graphene using near-field infrared nanoscopy. We observe various domain-wall structures in mechanically exfoliated graphene bilayers, including network-forming triangular lattices, individual straight or bent lines, and even closed circles. The near-field infrared contrast of domain-wall solitons arises from plasmon reflection at domain walls, and exhibits markedly different behaviours at the tensile- and shear-type domain-wall solitons. In addition, the plasmon reflection at domain walls exhibits a peculiar dependence on electrostatic gating. Our study demonstrates the unusual and tunable coupling between 2D graphene plasmons and domain-wall solitons.**

Bilayer graphene has attracted much research interest owing to its unique electronic<sup>14–17</sup> and optical properties<sup>18–20</sup>, such as unusual quantum Hall states and tunable semiconductor bandgaps. Two degenerate lowest-energy stacking orders AB and BA exist in bilayer graphene<sup>21</sup>, and one stacking order can transit to the other through shifting the top layer of graphene with respect to the bottom layer along the armchair direction (a transition dislocation vector)<sup>1,2</sup>. The region of transition between AB- and BA-stacked bilayer graphene domains forms a soliton-like 1D domain wall<sup>1–4</sup>. Bilayer graphene is the thinnest crystal that can confine a layer-stacking domain wall, providing an attractive 2D platform to explore the physics of domain-wall solitons. Different types of domain-wall soliton can exist in bilayer graphene depending on the soliton orientation relative to the transition dislocation vector: solitons parallel to the dislocation vector are characterized by a shear strain at the domain wall, whereas solitons perpendicular to the dislocation vector are characterized by a tensile strain. The unique 1D domain-wall solitons and their interactions with excitations in 2D bilayer graphene domains can lead to fascinating structural, electrical and optical properties. Structurally, the domain walls form nanometre-wide strain solitons with the width correlated with

the type of solitons<sup>1,2</sup>. Electrically, topologically protected quantum valley Hall edge states at the domain walls have been theoretically predicted<sup>5,7–11</sup> and experimentally observed<sup>6</sup>. Such edge states are present for all domain walls, but their microscopic electronic structure may vary markedly in different types of soliton. Optically, the domain-wall solitons give rise to remarkable local features that enabled direct visualization of the solitons by near-field infrared nanoscopy<sup>6</sup>. The physical origin of the local optical responses, however, is yet unknown. Here we report the observation of strong surface plasmon reflection at domain-wall solitons, which is quite unexpected because the electronic structure change is relatively smooth and weak over the layer-stacking domain walls compared with the abrupt and strong changes at graphene edges. This plasmon reflection is largely responsible for the near-field optical contrast of domain-wall solitons. More surprisingly, we find that a wide variety of soliton structures are present naturally in exfoliated bilayer graphene, and the plasmon reflection exhibits a striking dependence on the type of domain-wall solitons. In addition, the plasmon reflection at the domain-wall solitons can be controlled by electrostatic gating. These observations highlight the unique and rich physical behaviour at domain-wall solitons in bilayer graphene.

Figure 1a shows a schematic of the near-field infrared nanoscopy technique<sup>22–25</sup> in which an infrared light beam at  $\lambda = 10.6 \mu\text{m}$  was focused onto the apex of a conductive atomic force microscope (AFM) tip and the back-scattered light was collected for near-field imaging (see Methods and Supplementary Information for details of the technique). The topography and near-field nanoscopy images of a representative bilayer graphene with domain walls are shown in Fig. 1b,c, respectively. The topography image is largely featureless within the bilayer region (Fig. 1b). In contrast, the near-field image (Fig. 1c) shows many bright lines that arise from AB–BA domain-wall solitons across the bilayer region.

We observe a remarkable richness of domain-wall patterns in as-exfoliated bilayer graphene using near-field infrared nanoscopy, as illustrated in Figs 1c and 2. The most common patterns are relatively straight domain-wall solitons extending across a bilayer (Fig. 1c). However, sometimes we observe dense triangular lattices formed by meshes of domain-wall solitons (Fig. 2a), sharply bent L-shape solitons (Fig. 2b), or even solitons forming a closed-loop circle (Fig. 2c). These different domain-wall patterns provide a rich platform to explore solitons of different domain-wall configurations. Indeed, the high-resolution images in Fig. 2 show that the domain walls can exhibit very different near-field optical

<sup>1</sup>Department of Physics, University of California at Berkeley, Berkeley, California 94720, USA. <sup>2</sup>Institute of Physics, Chinese Academy of Sciences, Beijing 100190, China. <sup>3</sup>Physics Department, Tsinghua University, Beijing 100084, China. <sup>4</sup>Materials Science Division, Lawrence Berkeley National Laboratory, Berkeley, California 94720, USA. <sup>5</sup>Kavli Energy NanoSciences Institute at the University of California, Berkeley and the Lawrence Berkeley National Laboratory, Berkeley, California 94720, USA. <sup>†</sup>These authors contributed equally to this work. \*e-mail: [fengwang76@berkeley.edu](mailto:fengwang76@berkeley.edu)

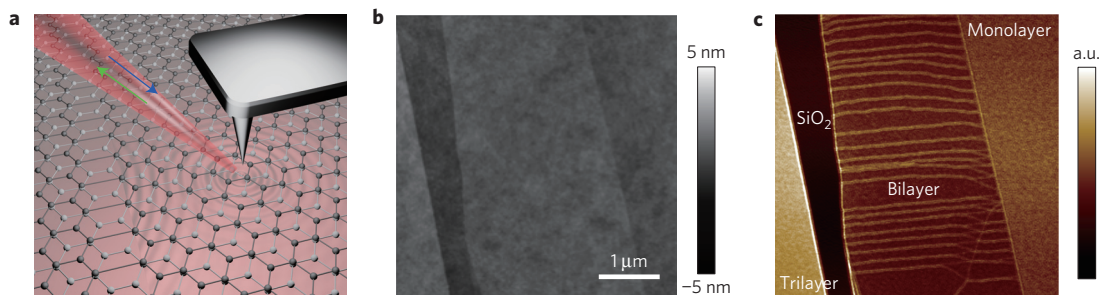


**Figure 1 | Nano-imaging of domain walls in bilayer graphene using the near-field infrared nanoscopy technique.** **a**, A schematic of the infrared nanoscopy technique, where an infrared laser with wavelength  $\lambda = 10.6 \mu\text{m}$  is focused at the apex of an AFM tip, and the local infrared responses are probed through the scattered light in the far field. The blue and green arrows illustrate the incident and scattered infrared light, respectively. **b**, AFM topography image of an exfoliated bilayer graphene on  $\text{SiO}_2/\text{Si}$  substrate showing a featureless bilayer graphene region. **c**, The near-field infrared image taken simultaneously with the AFM topography reveals prominent bright lines arising from the layer-stacking domain-wall solitons. The colour corresponds to the intensity of the scattered infrared light.

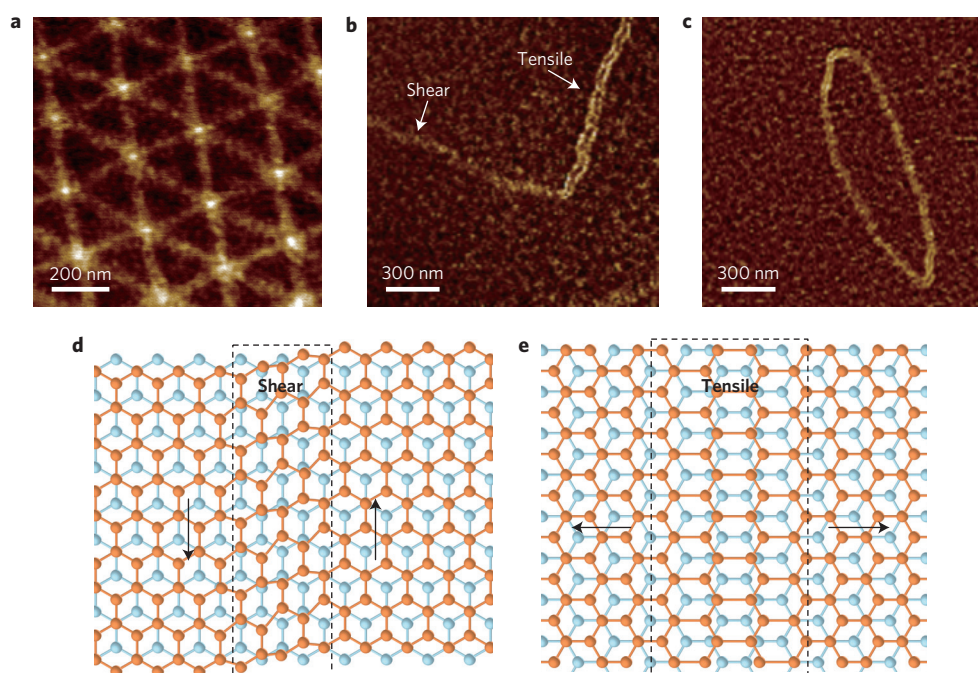


**Figure 2 | Near-field infrared images of a rich variety of bilayer graphene domain-wall structures.** **a**, A triangular lattice formed by the domain-wall network. All domain walls in the triangular network show the single-bright-line feature. **b**, A sharply bent L-shape domain wall. One segment shows the single-bright-line feature whereas the other segment rotated by  $90^\circ$  shows the double-bright-line feature, indicating different infrared responses. **c**, A closed-loop domain-wall circle. The single-bright-line segments (close to the vertical direction) and double-bright-line segments (close to the horizontal direction) appear alternately along the circumference. **d, e**, Schematics of the shear (**d**) and tensile (**e**) domain-wall solitons. The dashed lines outline the domain-wall region through which the AB-stacking domain smoothly transits to the BA-stacking domain. The arrows indicate the dislocation directions. For the shear soliton in **d**, the dislocation vector is parallel to the domain wall. For the tensile soliton in **e**, the dislocation vector is perpendicular to the domain wall.

features. In the dense triangular domain-wall network of Fig. 2a, all domain walls are characterized by one bright line in the near-field image. For the sharply bent L-shape domain wall in Fig. 2b, one segment shows one bright line, whereas the other segment at  $90^\circ$  shows a pair of two bright lines. This behaviour is most striking in the circular domain wall (Fig. 2c): the domain-wall segments close to the vertical direction feature one bright line, and the segments close to the horizontal direction feature double bright lines. We also notice that the single-bright-line feature is generally weaker than the double-bright-line feature. These results demonstrate unambiguously that domain-wall solitons along different orientations can have very different electronic structures and near-field optical responses at  $10.6 \mu\text{m}$  excitation.

To understand this unusual soliton-dependent optical behaviour, we first examine the microscopic structure of the possible domain-wall soliton configurations. AB- and BA-stacked bilayer graphene are two degenerate states with the lowest stacking energy<sup>21</sup>. To switch from AB to BA stacking, the top layer of graphene needs to shift relative to the bottom layer by a carbon-carbon bond length of  $1.42 \text{ \AA}$  along the armchair direction, defining a dislocation vector<sup>1</sup>. A change in the relative orientation of the domain-wall soliton and the dislocation vector leads to a different local structure at the domain wall. Figure 2d,e shows schematics of two limiting cases of the domain-wall soliton in bilayer graphene. Figure 2d shows a shear soliton, where the right (left) domain on the top layer of graphene shifts upward (downward) along the armchair orientation;

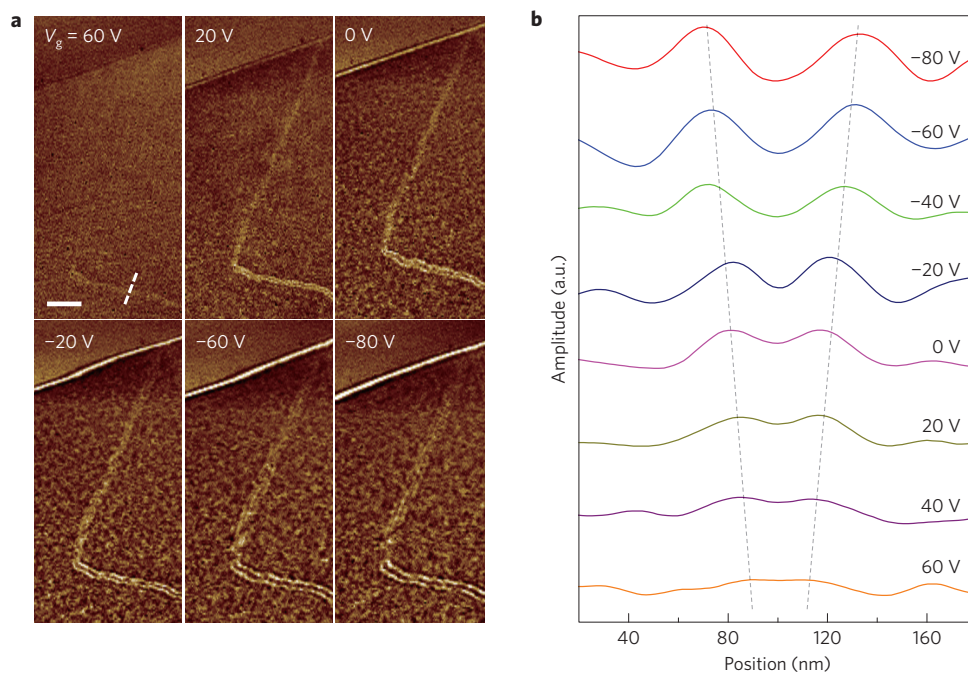


**Figure 3 | Gate-dependent surface plasmon reflection at domain-wall solitons.** **a**, Near-field infrared nanoscopy images of the layer edge, shear soliton and tensile soliton in a bilayer graphene at different gate voltages. The plasmon feature at the bilayer graphene edge disappears at gate voltage ( $V_g$ ) = 60 V, corresponding to the CNP, and it becomes stronger with longer plasmon wavelength with increased carrier density when the gate voltage is changed from 60 V to  $-80$  V. The near-field optical features at domain-wall solitons show related gate dependences: the feature is the weakest/non-observable for the tensile/shear soliton at the CNP. Away from the CNP, the double-bright-line feature at the tensile domain-wall soliton shows increased strength, and the line separation increases. For the shear domain-wall soliton, the single-bright-line feature becomes stronger with increased doping, and it evolves into three bright lines at  $V_g$  lower than  $-20$  V. These gate- and soliton-dependent features at bilayer graphene domain walls arise from unusual plasmon reflection behaviour at different types of domain wall. The scale bar is 300 nm. **b**, Gate-dependent plasmon interference profiles at the tensile soliton from a line cut in the near-field optical images (along the white dashed line in **a**). The two peaks, indicated by the dashed lines, correspond to the two bright lines, and their separation increases with the carrier density away from the CNP.

that is, the domain wall is parallel to the dislocation. Figure 2e shows a tensile soliton, where the right (left) domain on the top layer shifts left (right) along the zigzag direction; that is, the domain wall is perpendicular to the dislocation. Previous structural studies of the domain-wall soliton using high-resolution transmission electron microscopy (TEM) reveal that the shear and tensile solitons have different widths at 6 nm and 11 nm, respectively<sup>1</sup>. In addition, the TEM study shows that the six-fold symmetric triangular domain-wall networks are usually composed of only shear solitons.

The unusual near-field optical patterns of domain-wall solitons can be understood phenomenologically by assigning the single-bright-line and double-bright-line features to shear and tensile solitons, respectively. We measured three bilayer samples with triangular domain-wall networks like those in Fig. 2a, which are composed of shear solitons according to previous TEM studies<sup>1</sup>. All such domain walls in triangle networks show the single-bright-line feature with no exception. In Fig. 2b the two segments of the L-shaped domain wall have a  $90^\circ$  bend, corresponding to a shear to tensile soliton transition. Accordingly, the near-field optical contrast changes from a segment of single bright line to two bright lines. The circular soliton in Fig. 2c, by its topology, should have two shear soliton segments and two tensile soliton segments around its circumference, consistent with the observation of alternating single-bright-line and double-bright-line features around the circle. We note that domain-wall solitons between the shear and tensile segments should exhibit a smooth transition of electronic structure and near-field optical contrast, but our experiments are not able to probe these finer details. Statistically there are more domain walls characterized by a single bright line, consistent with the fact that the shear solitons have a slightly lower energy than the tensile solitons.

Next we investigate the physical origin of the near-field optical contrast of domain-wall solitons in bilayer graphene. The double-bright-line feature at tensile domain-wall solitons shows that the near-field optical responses are highly nonlocal. This feature can arise from reflection of 2D graphene plasmons, as observed at domain boundaries in monolayer graphene<sup>26</sup>. To test this surface plasmon reflection hypothesis, we studied the gate dependence of the domain-wall soliton feature because the properties of 2D graphene plasmons can be continuously tuned through electrostatic gating<sup>27–30</sup>.

Figure 3a shows the evolution of the near-field infrared image of a bilayer graphene containing a shear soliton, a tensile soliton, and a layer edge as the backgate voltage is varied from 60 to  $-80$  V. Gate-dependent plasmon responses in graphene and its reflection at layer edges have been extensively studied previously<sup>28–31</sup>. The wavelength and intensity of graphene plasmons increase monotonically with the carrier density induced by electrostatic gating. Consequently, the plasmon interference pattern at graphene edges becomes more pronounced and its period becomes longer as the charge density increases. In our experiment, we find that the edge plasmon disappears at  $V_g = 60$  V, corresponding to the charge neutral point (CNP). Away from the CNP, the edge plasmon feature becomes stronger and has a longer wavelength with increased doping (at decreased gate voltages). The near-field optical feature at the tensile domain wall exhibits a behaviour very similar to the edge plasmon: the double-bright-line feature is weakest at the CNP, and it becomes more pronounced and has a longer wavelength at higher doping (Fig. 3b). It demonstrates unambiguously that the double-bright-line feature at tensile domain walls in the near-field optical image is largely due to reflection of graphene plasmons. The near-field

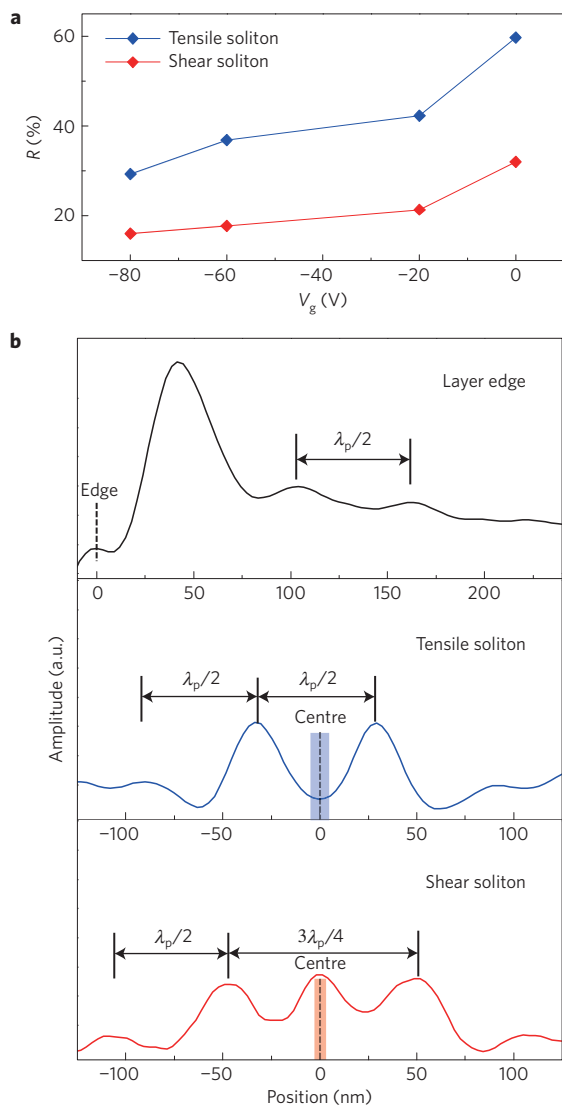


**Figure 4 | Plasmon reflectance and phase at the shear and tensile domain walls.**

**a**, Reflectance ( $R$ ) of plasmons at shear (red symbols) and tensile (blue symbols) domain walls as a function of the gate voltage ( $V_g$ ). The reflectance at a tensile soliton is always higher than that at a shear soliton. For both tensile and shear solitons, the reflectance decreases with increased carrier density (that is, more negative voltage). **b**, Plasmon interference profiles across the layer edge (top panel), tensile domain-wall soliton (middle) and shear domain-wall soliton (bottom) at  $V_g = -80$  V. The dashed line in the top panel represents the physical edge position of the graphene flake; the dashed lines in the middle and bottom panels represent the centre of the tensile and shear solitons, respectively. The shaded areas in the middle (blue) and bottom (red) panels label the structural widths of the tensile and shear solitons. The plasmon wavelength  $\lambda_p$  is determined to be 120 nm from the plasmon interference profile at the layer edge. Using this  $\lambda_p$  value, we obtained an effective reflection phase of  $\sim \pi$  at the tensile domain-wall soliton, giving rise to a destructive interference (that is, dark point) at the centre and a separation of  $\lambda_p/2$  between the two side peaks (middle panel). In contrast, the effective reflection phase is estimated to be  $\pi/2$  at the shear domain-wall soliton, giving rise to a separation of  $3\lambda_p/4$  between the two side peaks (lower panel).

optical feature around the shear domain wall (Fig. 3a) also shows a systematic gate dependence: the feature is unobservable at the CNP, and it gets brighter with increased doping. At gate voltages lower than  $-20$  V, two new parallel lines appear on the two sides

of the central bright line, and the separation of these lines increases with the gate voltage. This unusual gate dependence, including the disappearance of contrast at the CNP and the multiple-parallel-line feature at high gate voltages, indicates that the near-field optical contrast of shear solitons is also dominated by plasmonic reflection at the domain wall.

The distinct appearances of shear and tensile solitons suggest that plasmon reflection at the domain walls varies significantly at different type of solitons, presumably owing to their different local structures and electronic bands. The plasmon reflection can be characterized in general by the reflectance and phase: the reflectance determines the magnitude of the contrast, and the reflection phase determines the position of constructive interference (that is, the bright lines) in the near-field optical images. Both parameters are different for plasmon reflection at shear and tensile solitons.

We first examine the plasmon reflectance. It is obvious from Fig. 3 that the contrast at tensile solitons is stronger than that at the shear solitons for every gate voltage. The same behaviour was observed in all as-prepared samples without electrical gating. This stronger near-field contrast at tensile domain-wall solitons corresponds to higher reflectance. To be more quantitative, we can compare the domain-wall contrast to that of the layer edges, where the plasmon reflection is close to 100%. The reflectance then can be estimated as  $r = (s_{\text{DW}} - s_{\text{bulk}})/(s_{\text{edge}} - s_{\text{bulk}})$ , where  $s_{\text{DW}}$ ,  $s_{\text{edge}}$  and  $s_{\text{bulk}}$  are the near-field signal of the domain-wall bright line, the edge bright line, and the bulk background, respectively. Figure 4a shows the reflectance from both the tensile and shear solitons when the gate voltage varies from 0 to  $-80$  V. Apparently the plasmon reflectance is higher at tensile domain walls, and the reflection becomes weaker at both domain walls with increased carrier doping. Both behaviours can be understood qualitatively by considering the effects of domain-wall width and plasmon wavelength: the reflectance tends to be higher for wider domain walls and shorter plasmon wavelength. It has been shown in TEM studies that the domain-wall width of tensile solitons ( $\sim 11$  nm) is larger than that of shear solitons ( $\sim 6$  nm). Consequently, tensile domain walls can have stronger plasmon reflection. At higher carrier density the plasmon wavelength becomes longer, and the reflectance decreases for all types of soliton.

Next we examine the plasmon reflection phase. Figure 4b shows plasmon interference profiles at the layer edge, shear soliton, and tensile soliton at  $V_g = -80$  V. The profiles are averaged along the layer edge and the domain-wall solitons to increase the signal/noise ratio, so that weaker interference fringes become observable. The plasmon wavelength is determined to be  $\lambda_p \approx 120$  nm by measuring the peak-to-peak distance in the plasmon interference profile at the layer edge (top panel of Fig. 4b). In each side of the domain wall, the plasmon interference pattern is formed by tip-launched forward and soliton-reflected backward plasmon waves, which is similar to plasmon interference at graphene edges. Plasmon waves coming from both sides get reflected in the same way, and form a symmetrical interference pattern. Shear solitons and tensile solitons show very different behaviour: at the soliton position (that is, at the centre), the interference pattern exhibits a peak for shear solitons and a dip for tensile solitons. As the interference pattern is directly related to the reflection phase shift, different interference patterns indicate different reflection phase shifts for shear and tensile solitons. Empirically, we can define an effective phase shift  $\phi$  by  $\phi = 2\pi(1 - D/\lambda_p)$ , where  $D$  is the distance between two symmetric peaks. For tensile solitons,  $D_{\text{tensile}} \approx 0.5\lambda_p$  (Fig. 4b middle panel) indicates an effective phase shift of  $\sim \pi$ ; and for shear solitons  $D_{\text{shear}} \approx 0.75\lambda_p$  (Fig. 4b bottom panel) corresponds to an effective phase shift of  $\sim \pi/2$ . (Note that the peak in the centre of the shear domain wall does not correspond to an interference maximum because the reflection phase at the domain wall is not zero.)

A complete understanding of the unusual plasmon reflection at domain walls, including the evolution of its reflectance and phase with both electrostatic gating and soliton types, will provide much insight onto the unique properties of domain-wall solitons in bilayer graphene. We hope that our experimental findings will stimulate future theoretical investigations into this fascinating system.

In conclusion, we show that surface plasmon reflection at 1D domain walls enables visualization of a wide variety of domain-wall solitons in exfoliated bilayer graphene using near-field infrared nanoscopy. Such plasmon reflection exhibits strikingly different behaviour at shear and tensile domain walls. Our result provides a new avenue to manipulate 2D plasmons based on stacking domain-wall solitons, and represents a first example of unusual soliton-dependent coupling between 2D electrons/plasmons in graphene domains and 1D domain-wall solitons.

## Methods

Methods and any associated references are available in the [online version of the paper](#).

Received 14 December 2015; accepted 4 May 2016;  
published online 30 May 2016

## References

- Alden, J. S. *et al.* Strain solitons and topological defects in bilayer graphene. *Proc. Natl Acad. Sci. USA* **110**, 11256–11260 (2013).
- Butz, B. *et al.* Dislocations in bilayer graphene. *Nature* **505**, 533–537 (2014).
- Yankowitz, M. *et al.* Electric field control of soliton motion and stacking in trilayer graphene. *Nature Mater.* **13**, 786–789 (2014).
- Lin, J. H. *et al.* AC/AB stacking boundaries in bilayer graphene. *Nano Lett.* **13**, 3262–3268 (2013).
- Yao, W., Yang, S. A. & Niu, Q. Edge states in graphene: from gapped flat-band to gapless chiral modes. *Phys. Rev. Lett.* **102**, 096801 (2009).
- Ju, L. *et al.* Topological valley transport at bilayer graphene domain walls. *Nature* **520**, 650–655 (2015).
- Zhang, F., Jung, J., Fiete, G. A., Niu, Q. & MacDonald, A. H. Spontaneous quantum Hall states in chirally stacked few-layer graphene systems. *Phys. Rev. Lett.* **106**, 156801 (2011).
- Martin, I., Blanter, Y. M. & Morpurgo, A. F. Topological confinement in bilayer graphene. *Phys. Rev. Lett.* **100**, 036804 (2008).
- Zhang, F., MacDonald, A. H. & Mele, E. J. Valley Chern numbers and boundary modes in gapped bilayer graphene. *Proc. Natl Acad. Sci. USA* **110**, 10546–10551 (2013).
- Vaezi, A., Liang, Y. F., Ngai, D. H., Yang, L. & Kim, E.-A. Topological edge states at a tilt boundary in gated multilayer graphene. *Phys. Rev. X* **3**, 021018 (2013).
- Semenoff, G. W., Semenoff, V. & Zhou, F. Domain walls in gapped graphene. *Phys. Rev. Lett.* **101**, 087204 (2008).
- Hattendorf, S., Georgi, A., Liebmann, M. & Morgenstern, M. Networks of ABA and ABC stacked graphene on mica observed by scanning tunneling microscopy. *Surf. Sci.* **610**, 53–58 (2013).
- Lalmi, B. *et al.* Flower-shaped domains and wrinkles in trilayer epitaxial graphene on silicon carbide. *Sci. Rep.* **4**, 4066 (2014).
- Oostinga, J. B., Heersche, H. B., Liu, X. L., Morpurgo, A. F. & Vandersypen, L. M. K. Gate-induced insulating state in bilayer graphene devices. *Nature Mater.* **7**, 151–157 (2008).
- Dean, C. R. *et al.* Hofstadter's butterfly and the fractal quantum Hall effect in moire superlattices. *Nature* **497**, 598–602 (2013).
- Velasco, J. Jr *et al.* Transport spectroscopy of symmetry-broken insulating states in bilayer graphene. *Nature Nanotech.* **7**, 156–160 (2012).
- Novoselov, K. S. *et al.* Unconventional quantum Hall effect and Berry's phase of  $2\pi$  in bilayer graphene. *Nature Phys.* **2**, 177–180 (2006).
- Zhang, Y. *et al.* Direct observation of a widely tunable bandgap in bilayer graphene. *Nature* **459**, 820–823 (2009).
- Mak, K. F., Lui, C. H., Shan, J. & Heinz, T. F. Observation of an electric-field-induced band gap in bilayer graphene by infrared spectroscopy. *Phys. Rev. Lett.* **102**, 256405 (2009).
- Yang, L., Deslippe, J., Park, C.-H., Cohen, M. L. & Louie, S. G. Excitonic effects on the optical response of graphene and bilayer graphene. *Phys. Rev. Lett.* **103**, 186802 (2009).
- Aoki, M. & Amawashi, H. Dependence of band structures on stacking and field in layered graphene. *Solid State Commun.* **142**, 123–127 (2007).
- Keilmann, F. & Hillenbrand, R. Near-field microscopy by elastic light scattering from a tip. *Phil. Trans. R. Soc. A* **362**, 787–805 (2004).
- Novotny, L. & Hecht, B. *Principles of Nano-Optics* (Cambridge Univ. Press, 2006).
- Bechtel, H. A. *et al.* Ultrabroadband infrared nanospectroscopic imaging. *Proc. Natl Acad. Sci. USA* **111**, 7191–7196 (2014).
- Gerber, J. A., Berweger, S., O'Callahan, B. T. & Raschke, M. B. Phase-resolved surface plasmon interferometry of graphene. *Phys. Rev. Lett.* **113**, 055502 (2014).
- Fei, Z. *et al.* Electronic and plasmonic phenomena at graphene grain boundaries. *Nature Nanotech.* **8**, 821–825 (2013).
- Hwang, E. H. & Das Sarma, S. Dielectric function, screening, and plasmons in two-dimensional graphene. *Phys. Rev. B* **75**, 205418 (2007).
- Fei, Z. *et al.* Gate-tuning of graphene plasmons revealed by infrared nano-imaging. *Nature* **487**, 82–85 (2012).
- Chen, J. *et al.* Optical nano-imaging of gate-tunable graphene plasmons. *Nature* **487**, 77–81 (2012).
- Ju, L. *et al.* Graphene plasmonics for tunable terahertz metamaterials. *Nature Nanotech.* **6**, 630–634 (2011).
- Yan, H. *et al.* Tunable infrared plasmonic devices using graphene/insulator stacks. *Nature Nanotech.* **7**, 330–334 (2012).

## Acknowledgements

The near-field infrared nanoscopy measurements and plasmon analysis are supported by the Office of Basic Energy Science, Department of Energy under contract No. DE-AC02-05CH11231 (Sub-wavelength Metamaterial programme). The bilayer graphene domain-wall sample preparation and characterization are supported by the Office of Naval Research award No. N00014-15-1-2651 (device fabrication and characterization) and the National Science Foundation award No. DMR-1206512 (sample preparation). L.Jiang acknowledges support from the Chinese Academy of Sciences. T.J. acknowledges support from the NSF Graduate Research Fellowship Program under Grant No. DGE 1106400.

## Author contributions

F.W. and Z.S. conceived the project. L.Jiang, Z.S., T.J., B.Z. and L.Ju performed the near-field infrared measurements. C.J. and J.K. prepared the samples. L.Jiang, Z.S., S.W., J.-H.K., T.L. and F.W. analyse the data. All authors discussed the results and contributed to writing the manuscript.

## Additional information

Supplementary information is available in the [online version of the paper](#). Reprints and permissions information is available online at [www.nature.com/reprints](http://www.nature.com/reprints). Correspondence and requests for materials should be addressed to F.W.

## Competing financial interests

The authors declare no competing financial interests.

## Methods

**Near-field infrared nano-imaging.** Our infrared nano-imaging technique is based on tapping-mode AFM. An infrared light beam ( $\lambda = 10.6 \mu\text{m}$ ) was focused onto the apex of a conductive AFM tip. The enhanced optical field at the tip apex interacts with graphene underneath the tip<sup>22,23</sup>. The scattered light, carrying local optical information of the sample, was collected by a MCT (HgCdTe) detector placed in the far field. Near-field optical images with spatial resolution better than 20 nm can be achieved with sharp AFM tips. Such near-field images are recorded simultaneously with the topography information during our measurements.

**Samples and devices preparation.** Bilayer graphene samples were mechanically exfoliated from bulk graphite onto SiO<sub>2</sub>/Si substrate and identified using optical contrast with a conventional optical microscope<sup>32</sup>. Electrical contacts of Ti/Au (5/50 nm) for backgate devices were fabricated by shadow mask evaporation.

## References

32. Novoselov, K. S. *et al.* Electric field effect in atomically thin carbon films. *Science* **306**, 666–669 (2004).